Self-healing Pd₃Au@Pt/C core-shell electrocatalysts with substantially enhanced activity and durability towards oxygen reduction

Sang-Young Lee [a,b], Namgee Jung [c], Dong Yun Shin [d], Hee-Young Park [a], Docheon Ahn [e], Hyoung-Juhn Kim [a], Jong Hyun Jang [a], Dong-Hee Lim [d], Sung Jong Yoo [a,f,*]

[a] Fuel Cell Research Center, Korea Institute of Science and Technology (KIST), Seoul 02792, Republic of Korea
[b] Research Division, Environmental Technology Institute, COWAY, Seoul 08826, Republic of Korea
[c] Graduate School of Energy Science and Technology (GEST), Chungnam National University, Daejeon 34134, Republic of Korea
[d] Department of Environmental Engineering, Chungbuk National University, Cheongju 28644, Republic of Korea
[e] Beamline Department, Pohang Accelerator Laboratory, Pohang 37673, Republic of Korea
[f] Clean Energy and Chemical Engineering, Korea University of Science and Technology, Daejeon 34113, Republic of Korea

ARTICLE INFO

ABSTRACT

Pt shells were synthesized on Pd-based alloy-cores *via* the chemical reduction method. Pt shells containing 1, 2, or 3 layers were prepared by controlling the amounts of Pt precursor used during synthesis. The thicknesses of Pt shell layers were calculated using the difference in the particle size between core and core-shell nanocatalysts, as determined from Cs-corrected scanning transmission electron microscopy (Cs-STEM) data. The shape and elemental distribution in the core-shell structured nanoparticles were analyzed using line profiles and elemental mapping from Cs-STEM. High-resolution X-ray diffraction and X-ray photoelectron spectroscopy analyses suggested that the structural and electronic properties of core-shell nanocatalysts were dependent on the number of shell layers. The activity and durability of the core-shell nanocatalysts were analyzed by the electrochemical method. Accelerated durability tests (ADT) were conducted in the potential range of 0.6–1 V for 10000 cycles, and the mass and specific activities of ADT were shown to be stable for the carbon-supported core-shell nanocatalyst with two Pt shell layers (core@Pt[2](*)/C). In addition, excellent electrochemical performance was observed for the core@Pt[2]/C sample before and after the ADT compared to the commercial samples as well as other samples prepared in this study. Importantly, the optimized Pt usage demonstrated in this study would significantly contribute to the commercialization of proton exchange membrane fuel cells.

© 2017 Elsevier B.V. All rights reserved.

1. Introduction

Proton exchange membrane fuel cells (PEMFCs) are one of the important type of fuel cells that allows the direct conversion of chemical energy into electricity at high efficiencies PEMFCs utilize hydrogen and oxygen as reactants for producing electricity [1]. Over the last several years, significant attention has been paid towards developing high-efficiency nanocatalysts that enhance the oxygen reduction reaction (ORR) in PEMFCs. Among the various nanocatalysts for the ORR at the cathode of the PEMFCs, Pt has been widely used. However, Pt dissolves during the operation of PEMFCs and therefore, exhibits low mass activity compared to high ORR performance [2–5]. Furthermore, in view of the limited Pt resources on

Earth, many researchers have investigated methods for reducing the amount of Pt used in the catalyst by alloying with other transition metals [1,6–13] or by designing catalysts that have a Pt shell on a pure metal or alloy-core composed of other elements [14–16].

Studies have been conducted on alloy-core catalysts involving metals other than Pt because of the high costs of Pt. In particular, PdM (M=Fe, Co, Ni, Cu, Y, W, Sc, Au, etc.) alloy nanocatalysts have been investigated for achieving enhanced ORR activities [17–23]. In addition to reducing Pt utilization, the synthesis of nanocatalysts with core-shell structures has led to improved ORR activities. When Pt is deposited on different metal, compressive or tensile stresses can occur, owing to lattice mismatch [2,24]. The structural changes caused by Pt deposition would affect the electronic structure of the core-shell alloy, owing to d-band shifts [25–28]. Among the various types of alloys, the effect of Au on the stability and durability of the nanocatalysts has been investigated at various composition ratios between the core and surface materials using density functional

theory (DFT) calculations [29,30]. Furthermore, the alloy or core-shell catalysts not only enhance the ORR activity, but are also stable and durable under the operating conditions of PEMFCs.

Many researchers have investigated the synthesis of Pt monolayers on core-shell nanocatalysts. There are six key methods for the synthesis of such nanocatalysts that may be broadly categorized into chemical and electrochemical methods. The six methods include electrochemical dealloying [31–36], chemical (acid) leaching [37,38], adsorbate-induced segregation [39], thermal-induced segregation [10,40], heterogeneous colloidal synthesis [41,42], and underpotential deposition (UPD) of Cu followed by galvanic displacement [3,43–45]. Among the electrochemical method, galvanic displacement except to Pt shell on Pt-based alloy-core nanocatalysts is an important one. In particular, Adzic and coworkers fabricated Pt monolayer shell *via* UPD of Cu on a pure metal or alloy-core composed of other elements [3,43–45]. However, although galvanic displacement enables the preferential deposition of Pt on the core, the retention of Cu in the alloy-core may be difficult with their method [46]. In addition, during the process, the Pt shell is accompanied by additional shell layers as a result of the UPD of Cu and it is difficult to control this process on a bulk scale. In a previous study conducted by our group, Pt shells were fabricated on alloy-core nanoparticles *via* the typical chemical reduction [46]. The deposition of Pt was accomplished by the selective reduction of Pd in the Pd_3Cu core.

In the present study, we have attempted to control the amount of Pt in the shell layer using the chemical reduction method and have optimized the shell layer compositions from the points of view of activity and durability during the accelerated durability tests (ADT). The nano-scale electronic and compositional properties of the $Pd_3Au@Pt/C$ core-shell catalysts were measured using Cs-corrected scanning transmission electron microscopy (Cs-STEM) technique, X-ray diffraction (XRD) analysis, and electrochemical methods. With the cyclic voltammetry (CV) data measured using before and after ADT, the electrochemical surface areas (ESAs) of Pd and Pt were simultaneously measured, and the change of ESAs at various shell layer compositions were determined to the dominant dissolution of materials caused by ADT. The composition of the Pt shell layers on a Pd_3Au core was optimized for maximizing the mass and specific activity at 0.9 V, as well as for improving catalyst loading amounts on the electrode and ESA_{Pt}.

2. Experimental section

2.1. Materials

Palladium(II) acetylacetonate [$Pd(C_5H_7O_2)_2$, 99%], gold(III) chloride trihydrate [$HAuCl_4 \cdot 3H_2O$, ≥99.9%], chloroplatinic acid hydrate [$H_2PtCl_6 \cdot xH_2O$, ≥99.995%], anhydrous ethanol (C_2H_6O, ≥99.5%), oleylamine (OA) ($C_{18}H_{35}NH_2$, 70%), and borane *tert*-butylamine [$(CH_3)_3CNH_2 \cdot BH_3$] were purchased from Aldrich. Diethyle 1,4-dihydro-2,6-dimethyl-3,5-pyridine dicarboxylate [$C_{13}H_{19}NO_4$, 95%], which was used as a reducing agent, was purchased from TCI. All the chemicals were used without further purification.

2.2. Synthesis

Carbon-supported core nanoparticles (20 wt.% metal, 3:1 Pd/Au molar ratio) were prepared *via* the chemical reduction method using borane *tert*-butylamine in anhydrous ethanol at room temperature. Carbon black (Vulcan XC-72, 0.1 g) was dispersed in 100 mL of anhydrous ethanol in a sonic bath. Following this, OA was added to the dispersed carbon black solution in the sonic bath and the mixture was vigorously stirred for 30 min. Pd

(0.145 mmol) and Au (0.048 mmol) precursors, and borane *tert*-butylamine (1.937 mmol) were dissolved in anhydrous ethanol. The solution containing the metal precursors and reducing agent was quickly added to the carbon black solution at intervals of 30 min and the mixture was vigorously stirred overnight. The mixture was then washed with excess ethanol and the filtered catalyst was dried in vacuum oven at 60 °C. The heat-treatment procedure involved heating from room temperature to 200 °C at a rate of 10 °C/min, under air flow in a tube furnace, maintaining the samples at 200 °C, and subsequently cooling to room temperature. The air-treated cores were dispersed in anhydrous ethanol in a sonic bath for 30 min, and then vigorously stirred in an oil bath at 80 °C for 30 min. Pt precursor (0.058, 0.116, and 0.251 mmol) and the reducing agent (0.321, 0.641, and 1.282 mmol) were dissolved in anhydrous ethanol and these solutions were added to the core mixture at 30 intervals. The mixture was kept under stirring conditions for 2 h and then the solution was filtered, washed and dried again. Using the above process, nanocatalysts with core to shell molar ratios of 1:0.3, 1:0.6, and 1: 1.3 were synthesized.

2.3. Catalyst characterization

Inductively coupled plasma (ICP-OES) spectrometry measurements were conducted for the catalysts with various molar ratios using the Thermo iCAP 6300 series instrument. Transmission electron microscopy (TEM) images obtained with the Philips CM30 were used to confirm the distribution and size of core and core@Pt[X] (X = 1, 2, and 3)/C core-shell nanoparticles. Cs-corrected scanning transmission electron microscopy (Cs-STEM) and EDX mapping images and line profiles of core@Pt[X]/C core-shell nanoparticles were acquired using the Jeol JEM-ARM200F instrument. X-ray diffraction (XRD) patterns were measured on a Rigaku D/MAX 2500 equipped diffractometer with a Cu Kα X-ray source (λ = 1.5401 Å). High resolution synchrotron powder X-ray diffraction (HR-PXRD) measurements of the core@Pt[X]/C nanocatalysts were carried out at the 9 B beamline of the Pohang Accelerator Laboratory (PAL). The incident X-rays were vertically collimated using a mirror and monochromatized to the wavelength of 1.5474 Å using a double-crystal Si (111) monochromator. The detector arm of the vertical scan diffractometer comprises of seven sets of Soller slits, flat Ge (111) crystal analyzers, antiscatter baffles, and scintillation detectors, with each set separated by 20°. Each sample of ca. 0.2 g powder was prepared by a flat-plate side-loading method to avoid a preferred orientation, and the sample was then rotated about the normal to the surface during the measurement, in order to increase the sampling statistics. A step scan was performed at room temperature from 2θ of 10° in 0.02° increments and overlaps the next detector bank up to a 2θ of 131°. In order to accurately determine the lattice parameters of the Pt shell phases in the core@Pt[X]/C nanocatalyst. HR-PXRD patterns were fitted by the whole-pattern profile matching method and the system was modeled by assuming multiple phases. The fitting procedure used is as follows. The lattice parameters of core and C in the core/C composited were determined from the first whole pattern profile matching with the HR-PXRD pattern. The lattice parameters obtained for the core and C were fixed and the lattice parameter of Pt in the core@Pt[X]/C was then fitted using whole-pattern profile matching of the HR-PXRD patterns. The effect of core-shell bulk structure and electronic configuration of platinum oxide component were investigated X-ray absorption near-edge spectroscopy (XANES). XANES results were gathered with extended X-ray absorption fine structure (EXAFS) facility installed at the 8C beam line in the PAL with ring current 200 mA, 3 GeV at PAL. EXAFS data were processed in the normal manner to obtain the absorbance values and analyzed with ATHENA and ARTEMIS in the IFEFFIT software suite. The current spectra of all samples were calibrated with a Pd foil in front of the

third ion chamber simultaneously and the spectra were acquired in the transmission mode using a gas ionizing detector at room temperature. Au 4f, Pd 3d and Pt 4f X-ray photoelectron spectroscopy (XPS) spectra were measured using a PHI-5000 Versa Probe (Ulvac PHI) and the binding energies were calibrated with respect to the C 1s peak at 284.6 eV. The XPS peaks were fir using the XPSPEAK 4.1 version program.

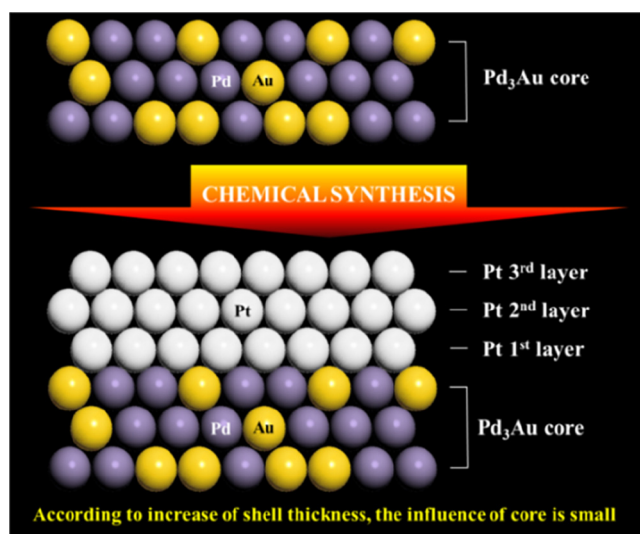## 2.4. Electrochemical measurements

All the electrochemical measurements (Auto lab 302N potentiostat) were carried out using a standard three-electrode cell comprising of a glassy carbon (GC) rotating disk electrode (RDE, 5 mm diameter), Pt wire, and saturated calomel electrode (SCE) as the working, counter, and reference electrodes, respectively. All the potentials are reported against the reversible hydrogen electrode (RHE). The desired ratio of catalyst ink slurry was prepared using 10 mg of catalyst, 0.1 mL of 5 wt.% Nafion solution (Aldrich), and 1 mL of 2-propanol. A single drop of prepared catalyst ink slurry was loaded onto GC substrate and dried in an oven. All the electrochemical measurements were conducted in the potential range of 0.05–1 V. Before the ORR measurements, cyclic voltammetry (CV) measurements were conducted under an Ar atmosphere in 0.1 M HClO$_4$ (perchloric acid, ACS reagent, 70%, Aldrich) for 30 min at a scan rate of 20 mV/s, in order to calculate the ESA of Pt in the core-shell catalyst. For this calculation, the hydrogen desorption peak of Pt with a charge density of 210 μC cm^{-2} was obtained. Next, ORR test was conducted under saturated O$_2$ atmosphere in HClO$_4$ for 30 min with a scan rate of 5 mV/s and a rotating rate of 1600 rpm. In addition, Blank CV, as ORR measurement condition under an Ar atmosphere, was measured and this data was used for correcting the other ORR data. CO$_2$ adsorption (CO$_{2ad}$) oxidation measurements were conducted for 5 min at 0.08 V to investigate CO$_2$ adsorption on the core-shell catalyst. The electrochemical cell was then saturated with Ar by purging for 30 min. The CO$_2$ adsorbed on the core-shell catalyst surface was stripped at a scan rate of 20 mV/s. The long term stability of core-shell catalyst was evaluated with ADT from 0.6 V to 1 V at a scan rate of 50 mV/s for 10000 cycles. After ADT measurement, all the electrochemical tests were repeated under the same conditions.

2.5. Computational methodology

Spin-polarized DFT calculations were performed using the Vienna *ab initio* Simulation Package (VASP) [47–50] with the projector-augmented wave (PAW) [51,52] method. Generalized gradient approximation (GGA) was used as the electron exchange-correlation functional and the Perdew, Burke and Ernzerhof (PBE) [53] model was used for the nonlocal corrections. A kinetic energy cutoff of 400 eV was used with a plane-wave basis set.

A rhombus-shaped 5.66 × 5.66 × 30.0 Å supercell with periodic boundary conditions was used for the Pt/Pd$_3$Au(111) surface systems. The vacuum space was set to be greater than 16.2 Å. The Pd$_3$Au(111) surface was constructed using a (2 × 2) surface unit cell and consisted of four layers. The Pt/Pd$_3$Au(111) surface was modeled by adding two layers on top of the Pd$_3$Au(111) surface, as described in Fig. 6. Brillouin zone integration of the surface was carried out using an 8 × 8 × 1 Monkhorst-Pack grid [54] and first-order Methfessel-Paxton smearing [55] with a width of 0.1 eV. The atoms in the bottom two layers of Pt/Pd$_3$Au(111) surface system were fixed at equilibrium lattice positions, while the other layers were fully relaxed. The surface systems were optimized until the total energy change for two steps of the electronic self-consistent loop less than 10^{-4} eV.

E_{vac} (i.e., the energy required to break the bond between the atoms of the Pt surface) for the top layer of the Pt/Pd$_3$Au(111) sur-

Scheme 1. Schematic illustration of the chemical synthesis of the core-shell nanoparticles.

face system was used as a measure of surface stability. E_{vac} was calculated using the following equation:

$$E_{vac} = E_{def} - E_{ref} + E_{bulk}$$

where, E_{def} is the total energy of the surface system containing one Pt vacancy, E_{ref} is the total energy of surface systems with no vacancy, and E_{bulk} is the total energy per Pt atom in the bulk (consisting of 4 atoms).

3. Results and discussion

3.1. Structure and morphology

A schematic illustration of the Pt shell layers deposited on the core by chemical synthesis is shown in Scheme 1. Using ICP-OES measurements, the average Pd/Au molar ratio of the synthesized cores was determined to be 2.91:1. In addition, the core nanoparticles were found to be dispersed uniformly on the carbon support for samples with and without heat-treatments, as indicated by the TEM images shown in Fig. S1 (see Supporting information). The uniform dispersion of the nanoparticles may be attributed to the use of OA, which is a surfactant and a versatile capping agent used widely for the synthesis of highly monodisperse metals [56]. The average particle size was determined by measuring the dimensions of ca. 100 particles in the TEM images. The average particle size of the cores without heat-treatment decreased with increase in the amount of OA. For samples synthesized with 1, 1.5, and 2 mL of OA (denoted as core/C OA 1, core/C OA 1.5, and core/C OA 2, respectively), the average particle sizes were 2.81 ± 0.19, 1.31 ± 0.09, and 0.95 ± 0.09 nm, respectively. Core/C OA 1, which had an appropriate size, was selected for heat-treatment. In addition, the average particle size also increased with increase in the duration of heat-treatment (3.56 ± 0.24, 4.78 ± 0.29, and 5.93 ± 0.35 nm for heat-treatment durations of 0.5, 1, and 1.5 h, respectively. The three samples are denoted as core/C OA 1 A 0.5, core/C OA 1 A 1, and core/C OA 1 A 1.5, respectively, hereafter).

The alloy-core samples were synthesized in three batches and the prepared cores were found to have typical face-centered cubic (fcc) structures, as determined from the XRD patterns (Fig. S2). The core (220) reflection peaks before and after heat-treatment were found at 65.10°, 65.12°, 65.18°, 65.52°, 65.60°, and 65.72° for core/C OA 1, core/C OA 1.5, core/C OA 2, core/C OA 1 A 0.5, core/C OA 1 A 1, and core/C OA 1 A 1.5, respectively. The peak positions of all the
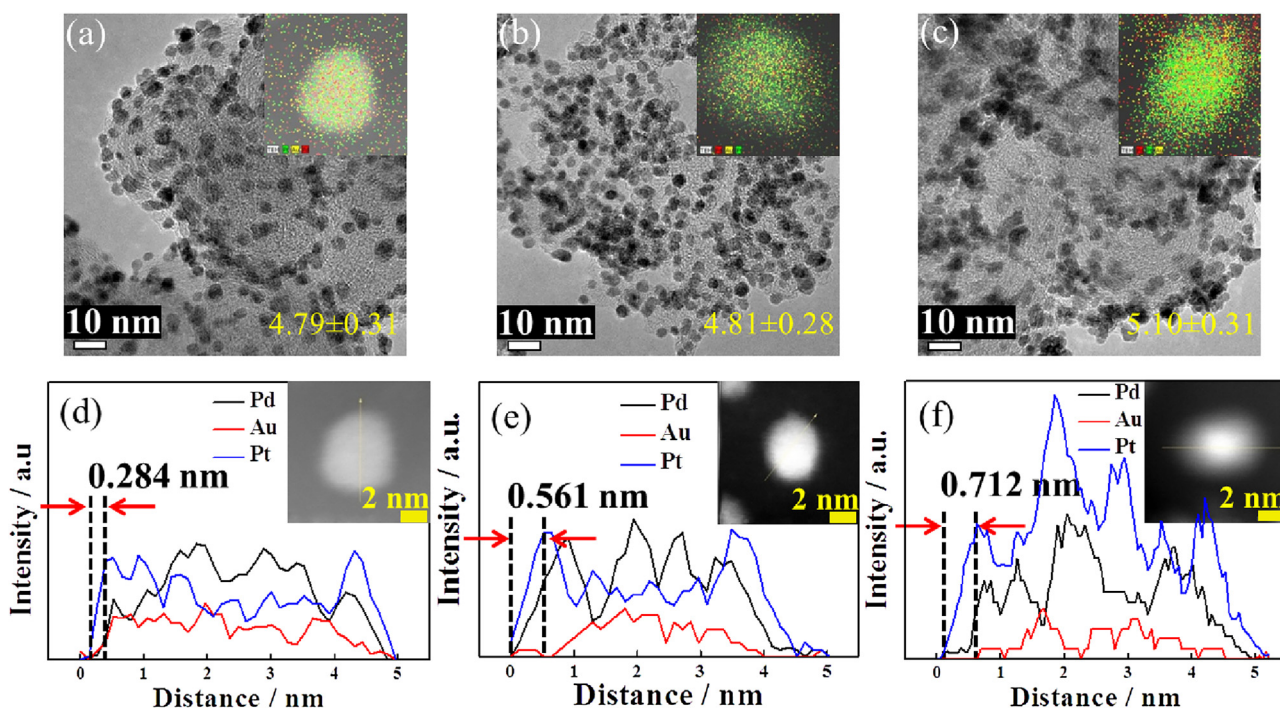
Fig. 1. Cs-STEM images (a)–(c) and line compositional profiles (d)–(f) of (a), (d) core@Pt[1]/C; (b), (e) core@Pt[2]/C; (c), (f) core@Pt[3]/C before ADT. Inset images of (a)–(c): elemental mapping by HAADF/STEM (red-Pd; yellow-Au; green-Pt). (For interpretation of the references to colour in this figure legend, the reader is referred to the web version of this article.)

core samples before heat-treatment were similar. With increase in the heat-treatment duration, the peak positions shifted in the positive direction as a result of the increase in crystallinity. In addition, all the XRD patterns were shifted in the negative direction owing to carbon contamination of Pd [57]. The crystallite size and lattice parameters of the cores with and without heat-treatment were calculated from the (220) diffraction peaks using the Debye-Scherrer equation (Table S1). While, the crystallite size increased with heat-treatment, the lattice parameters were unchanged, since the bulk composition was unchanged.

Fig. S3 shows the effect of impurities on the catalytic activities of the synthesized core/C nanocatalysts, as determined by CV and ORR measurements. The redox reactivity determined from the CV curves was significantly affected by the duration of heat-treatment. Before heat-treatment of core/C OA 1, the catalyst exhibited almost no activity, owing to the presence of the capping agent. However, after heat-treatment for 0.5–1.5 h, catalytic activity was gradually observed. In particular, redox reactivity was clearly observed after heat-treatment for over 1 h. Similarly, the ORR measurements of the samples with heat-treatment for over 1 h indicated significantly higher activity compared to the other samples. In addition, the kinetic current of the core/C OA 1 A 1 sample at 0.85 V was around 7 times higher compared to the core/C OA 1 A 0 sample. Therefore, we selected the core/C OA 1 A1 sample as the final appropriate state for the core-shell nanocatalyst.

The theoretical thickness of Pt shell layer was calculated using the following equation [58,59]:

$$D_{Pt-core} = D_{core} \left(1 + \frac{V_m(Pt)[Pt]}{V_m(core)[core]}\right)^{\frac{1}{3}}$$

In this equation, $D_{Pt-core}$ is the diameter of the core@Pt[X] shell nanoparticles, D_{core} is the diameter of the carbon supported core nanoparticles, V_m is the molar volume, [] is the atomic ratio between Pt and core (for Pt[1] − core, [Pt]/[core] = 1). Based on the particle size of Pt[X] − core, the deposited Pt shells determined

to contain single, double, and triple shell layers. According to the number of shell layers, the core-shell nanocatalysts are denoted as core@Pt[1]/C, core@Pt[2]/C, and core@Pt[3]/C.

The particle size, EDX compositional mapping, and line profile of the core-shell nanocatalysts were measured by Cs-STEM and the results are presented in Fig. 1. The bright images (a), (b), and (c) from Cs-STEM shown in Fig. 1 obtained before ADT, indicate that the average particle size distributions (Fig. S4) were 4.79 ± 0.31, 4.81 ± 0.28, and 5.10 ± 0.31 nm for Pt shells with single, double, and triple layers, respectively. The compositional distributions of Pd, Au, and Pt in all the core-shell nanocatalysts were determined from EDX coupled with HAADF/STEM images. These results confirm that the nanoparticles were dispersed uniformly in the catalyst. The existence of core-shell structures was confirmed from the line profiles in the HAADF/STEM images in Fig. 1(d), (e). The characteristic crown shape of the core-shell structure was definitely observed between the edges of the particles, except in the case of the core/Pt[3]/C sample. Through many amounts of Pt, core@Pt[3]/C sample is laminated such as Pt catalyst, and the deposition process is expected to influence the roughness of the surface. It is well-known that the atomic radius of Pt is around 0.139 nm. The thicknesses of the single, double, and triple Pt shell layers were measured to be 0.284, 0.561, and 0.712 nm, respectively.

As shown in the HR-PXRD patterns of core@Pt[X]/C (Fig. S5), the peaks for the core and Pt with fcc structures were found to be superimposed on each other. In the case of the Pt peaks, the peak intensity increased with increase in the amount of Pt (Fig. 2).

In addition, the Pt peak moved to higher 2θ values with increase in the amount of Pt, implying that the lattice parameter of the Pt fcc structure decreased with increase in the number of Pt shell layers. The peaks of the core@Pt[3]/C nanocatalyst were located at the same posi (220) phase of the Pt shell layers in the core@Pt[X]/C nanocatalysts were located at 2θ values of 67.50°, 67.58°, and 67.66° for core@Pt[1]/C, core@Pt[2]/C, and core@Pt[3]/C, respectively. With increase in the amounts of Pt, the Pt (220) reflection
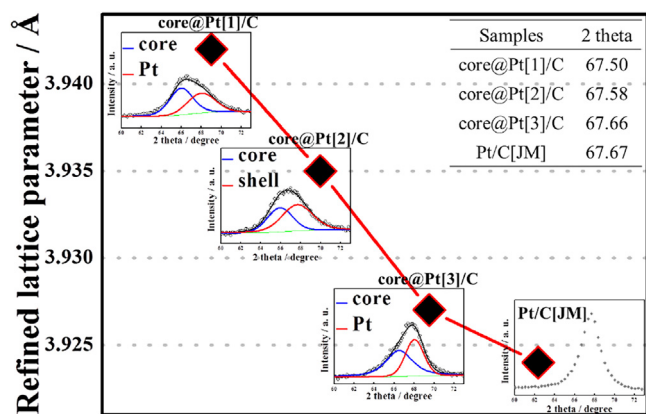
Fig. 2. Rietveld refined lattice parameters of the carbon-supported core@Pt[x]/C nanocatalysts and commercial Pt/C (Insets show synchrotron HR-PXRD patterns and 2 theta values of (220) reflection peaks).

peak was shifted towards Pt of Pt, the Pt (220) reflection peak was shifted towards Pt [JM] (67.67°, which is the experimentally measured value). Lattice relaxation and contraction of the Pt shell on the alloy-core for high and low loading of Pt, respectively, were examined by investigating the changes in the Pt lattice parameters. HR-PXRD measurements were conducted and fitted for accurately determining the Pt lattice parameter *via* the whole-pattern profile matching method. The bulk Pt lattice parameter is known to be 3.823 Å. The lattice parameters of the Pt layers on the core substrate were measured to be 3.942 ± 0.0002, $3.935n \pm 0.0002$, and 3.927 ± 0.0002 Å for core@Pt[1]/C, core@Pt[2]/C, and core@Pt[3]/C, respectively. Further, the lattice mismatch between the alloy-core and the Pt shells with 1, 2, and 3 layers were 2.08, 2.25, and 2.48%, respectively.

The electronic properties of the core and core@Pt[X]/C nanocatalysts were measured using XPS (Fig. S6). As shown in Fig. S6(b), (c), the Pd 3d (335.9 eV) and Au 4f

(83.4 eV) binding energies (BE) of the alloy-core in the core@Pt[X]/C nanocatalysts were lower than those of commercial Pd/C (336.9 eV) and Au/C (84.4 eV). The shifting of BE to lower values in the Pd/Au alloys is consistent with the results of the previous study [60,61]. The oxidation states and relative intensities of the core-alloys (Pd 3d and Au 4f) in the core@Pt[X]/C nanoparticles did not influence the interference of the Pt 4d 3/2 (332.2 eV) and Pt 4f 5/2 (74.50 eV) peaks. As shown in Fig. S6(a) the Pt 4f peak intensities of core@Pt[X]/C increased with increase in the amount of Pt, similar to the XRD results. In addition, the Pt 4f peaks were shifted to positive values compared to Pt/C [JM] in all the cases, except for the core@Pt[3]/C sample. In the XPS results for the core materials, the Au 4f peak of the core did not shift relative to core@Pt[X]/C. In contrast, the Pd 3d peaks for all the core@Pt[x]/C samples shifted in the negative direction by 0.2 eV. Interestingly, the Pd 3d peaks of core@Pt[1]/C, core@Pt[2]/C, and the Pt 4f peaks of core@Pt[1]/C, core@Pt[2]/C were found to shift by a constant value, indicating that the electronic properties of the core@Pt[1]/C and core@Pt[2]/C samples were affected by core. The electronic properties of the core and shell were different for samples with single and double Pt shell layers. As mentioned above, although a shift in the Au 4f 7/2 peaks was not observed, the Pd 3d 5/2 peaks of the core@Pt[X]/C sample were shifted to lower values compared to the core OA 1 A 1 sample. Thus, the positive shift in the BE for the Pt shell is consistent with the net charge required for extracting *d*-electrons from Pd. The XPS results are summarized in Table S2.

Fig. S7 shows the Pt L_{III} edges XANES for commercial Pt/C and core@Pt[2]/C nanocatalysts. A significant difference was observed between the curves of the various samples in the XANES region. This

indicates that the lattice mismatch and altered electronic states between Pd and Au of the core in core@Pt[2]/C affected the deposition of the Pt shell. Unfortunately, the specific Pt and Au peaks in the EXAFS region did overlap.

The average particle sizes of core@Pt[1]/C, core@Pt[2]/C, and core@Pt[3]/C were measured to be 4.75 ± 0.29, 4.83 ± 0.30, 5.18 ± 0.35 nm, respectively (Fig. S8). In order words, the particle size of core@Pt[1]/C after ADT was decreased by about 0.05 nm than before decreased by about 0.05 nm than before ADT, core@Pt[2]/C did not exhibit a significant difference in particle size, and the particle size of core@Pt[3]/C before ADT increased by about 0.08 nm after ADT. Pd, Au, and Pt were uniformly distributed in the catalyst particles in core@Pt[X]/C, as indicated by HAADF/STEM-EDX dark field images. The compositional line profiles show that the crown structure was maintained in all the samples after ADT. However, the intensity of Pd in core@Pt[1]/C decreased to larger until Au intensity due to the dissolution of Pd. In addition, the slight particle size reduction observed in the STEM bright image and decrease in the intensity of Pd in the line profile of core@Pt[1]/C expect

to indicate the porous nature of the core, which is a result of Pd dissolution. As a result, Au is exposed from the segregated core. The core@Pt[2]/C sample did not show significant difference after ADT. On the other hand, the intensity of Pt in the shell layer in the core@Pt[3]/C sample significantly decreased after 10,000 ADT cycles, and the sample changed to a crown shape compared to the shape observed before ADT. The particle size of the core@Pt[3]/C sample increased compared to the sample before ADT, shown in Fig. 1. The increase in the particle size is consistent with the Gibbs-Thomson energy relation of pure Pt/C [59]. Interestingly, comparison between Figs. 1 and 3 shows core material segregation of core@Pt[2] and [3]/C after ADT, owing to the change in the free energy of the alloy materials [62]. In a previous study by Adzic and coworkers, the effect of exposed Au on surface was attributed to the 'healing effect' [29]. However, it is clear that the structural changes occurred after ADT and would influence the electrochemical measurements.

3.2. Electrochemical characterizations

The electrochemical CV, ORR, and CO_{2ad} oxidation curves are summarized in Table S3. The CV curves in the range of 0.05 V-1 V(Fig. S9) confirm that, the particle size was reduced and the structure was changed after ADT for core@Pt[1]/C. These changes were accompanied by an increase in ESA. The ESA was calculated based on the hydrogen desorption region of Pd or/and Pt and the ESA variations of before and after ADT were estimated to be 12.20, −4.05, −17.33, and −33.65% for core@Pt[1]/C, core@Pt[2]/C, core@Pt[3]/C, and Pt/C[JM] samples, respectively. As shown for the core@Pt[1]/C nanocatalyst, the typical β-phase peak of Pd was observed around 0.06 V, owing to the reactions between the Pt atoms of the Pt monolayer on the Pd sites [63]. In addition, these reactions cause the inner core to be porous, as a result of the dissolution of Pd exposed between Pt atoms during ADT. Although porosity is not observed in the STEM images for samples subjected to up to 10,000 ADT cycles. Though specific peak of Au in core (Fig. S10) was shown around 1.1 V, core@Pt[1]/C before and after ADT was not shown. Therefore, the complete formation of Pt monolayer on core before ADT, and the maintaining of core-shell structure after ADT were confirmed. However, continuous ADT, it is expected that would be finally destroyed in the core-shell structure because of Pd dissolution. In contrast, the ESA of the core@Pt[3]/C decreased, owing to the agglomeration of individual particles, and Pt, rather than Pd, which first dissolves from the surface during electrochemical measurements.

The results of the ORR measurements before and after ADT are shown in Fig. S11. The half wave potentials ($E_{1/2}$) of the
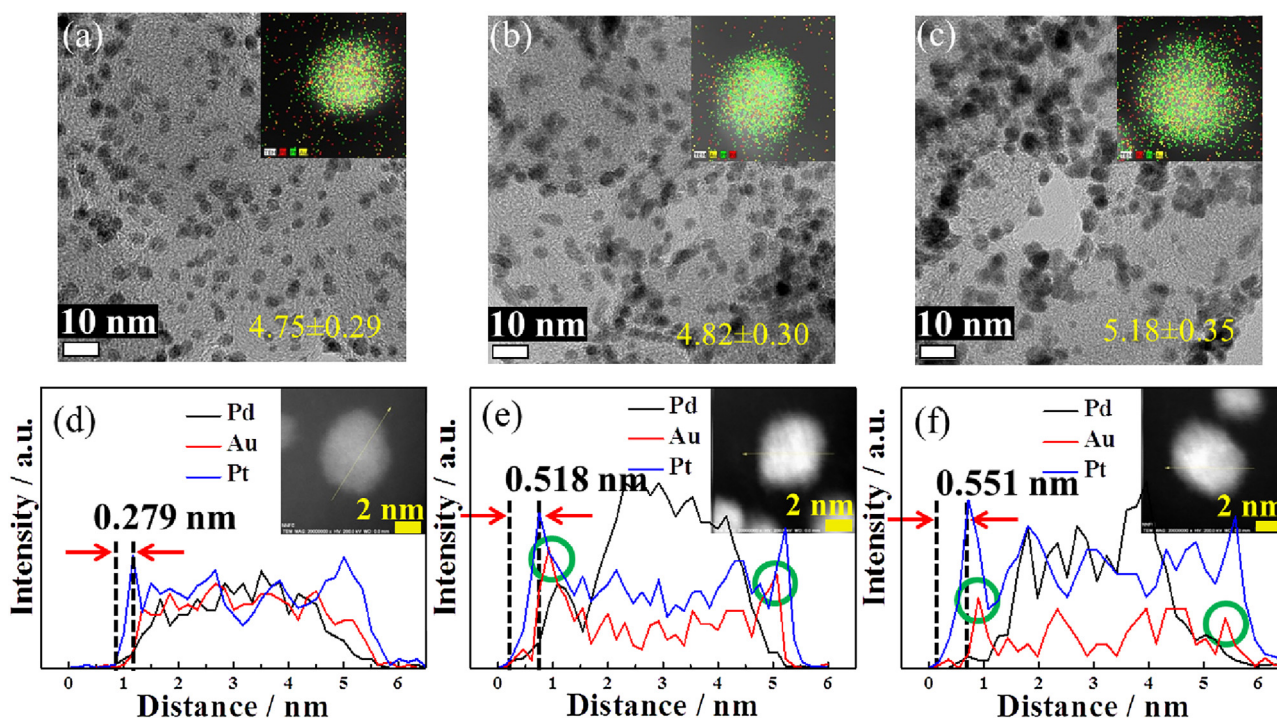
Fig. 3. Cs-STEM images (a)–(c) and line compositional profiles (d)–(f) of (a), (d) core@Pt[1]/C; (b), (e) core@Pt[2]/C; (c), (f) core@Pt[3]/C after ADT. Inset images of (a), (b), (c): elemental mapping by HAADF/STEM (red-Pd; yellow-Au; green-Pt). (For interpretation of the references to colour in this figure legend, the reader is referred to the web version of this article.)

core@Pt[X]/C nanocatalysts were found to be 0.899, 0.910, 0.913, and 0.903 V before ADT and 0.897, 0.910, 0.910, and 0.889 V after ADT for core@Pt[1]/C, core@Pt[2]/C, core@Pt[3]/C, and Pt/C [JM], respectively. The $E_{1/2}$ values after ADT were lower than those before ADT in most of the cases, except for the core@Pt[2]/C sample. Although weak core-shell interactions in core@Pt[1]/C catalyst caused Pd dissolution, the relative slight performance decrease was observed. The performance of the core@Pt[3]/C nanocatalyst, however, showed a different tendency for a Pt shell with a single layer. The reasons for this are expected to be related to differences in Pt dissolution and particle size effects.

Fig. 4, S12 show the CO_{2ad} oxidation curves at selected Pt areas on the surface [64,65]. The core@Pt[3]/C nanocatalyst exhibited two definite CO_{2ad} oxidation peak shifts after ADT, owing to the interactions between the core and shell. In the case of the core@Pt[3]/C nanocatalyst, after ADT, the maximum peak in CO_2 oxidation curve was shifted to 0.745 V from 0.725 V. This result directly showed that the properties of the Pt shell resembled the bulk state beyond three layers.

The Pt group metal (PGM) and Pt-based mass activities ($j_{k@0.9}V \rightarrow v$ values/PGM or Pt loading amount), and specific activities ($j_{k@0.9}V \rightarrow v$,mass values/ESA_{Pd+Pt} or ESA_{Pt} calculated from CV or CO_2 oxidation, respectively) of before and after ADT are shown in Fig. S13 to illustrate the relationships between ESA, CO_{2ad} oxidation area, and ORR measurement values. In addition, the values of mass and specific activities are summarized in Table S4. The core@Pt[2]/C nanocatalyst showed excellent PGM-based mass activity and the difference before and after ADT was about 2%. In addition, the Pt-based mass activity of the core@Pt[1]/C nanocatalyst was excellent. However, the core@Pt[2]/C nanocatalyst exhibited a light (about 3%) decline in mass activity. In contrast, the PGM and Pt-based specific activities of core@Pt[2]/C after ADT were increased by about 1 and 6%, respectively, compared with the values before ADT.
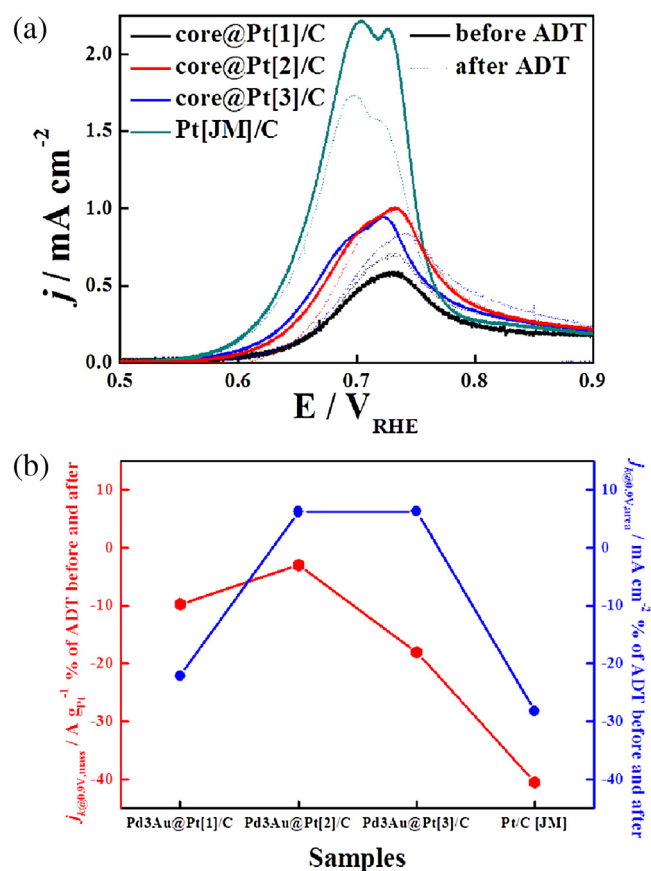

Fig. 4. Electrochemical measurements in 0.1 M $HClO_4$ (a) CO_{2ad} oxidation curves for core@Pt[x]/C and Pt[JM]/C of before(solid) and after(dot) ADT, (b) mass and specific activity variation% of before and after ADT at 0.9 V.
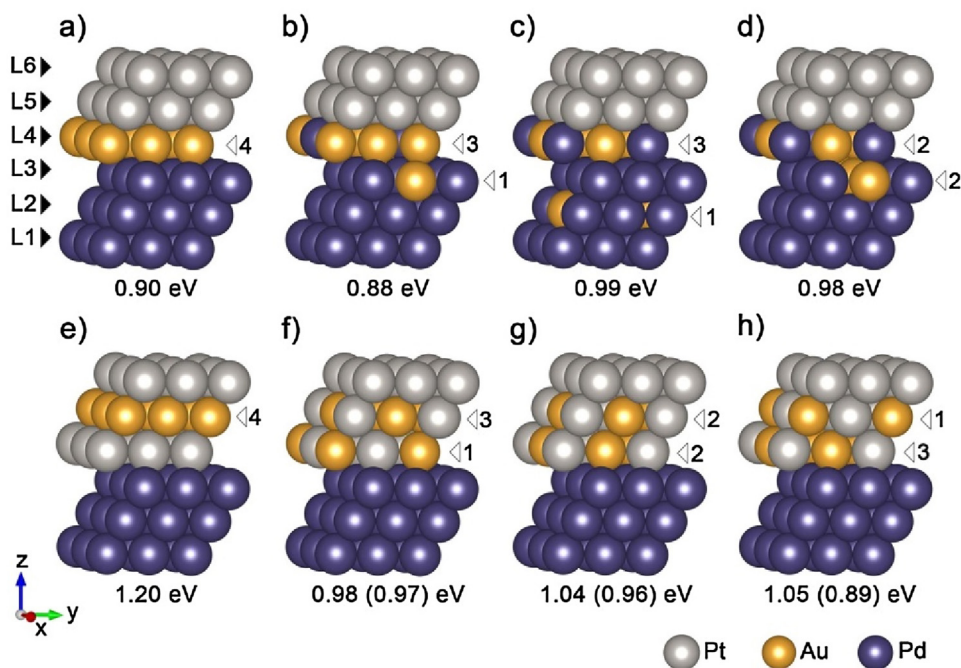
Fig. 5. Side views of modified Pt/Pd$_3$Au(111)–(2 × 2) surfaces with the Pt vacancy formation energies (E_{vac}) in eV. The values in parentheses indicate the E_{vac} at another location on the Pt vacancy site. L1 ∼ L6 indicate the various atomic layers. Numbers proceeded by hollow triangles (◁) represent the number of Au atoms in the layer. Note that periodic images are shown for each model, which may lead to misunderstanding the number of Au atoms in the images.
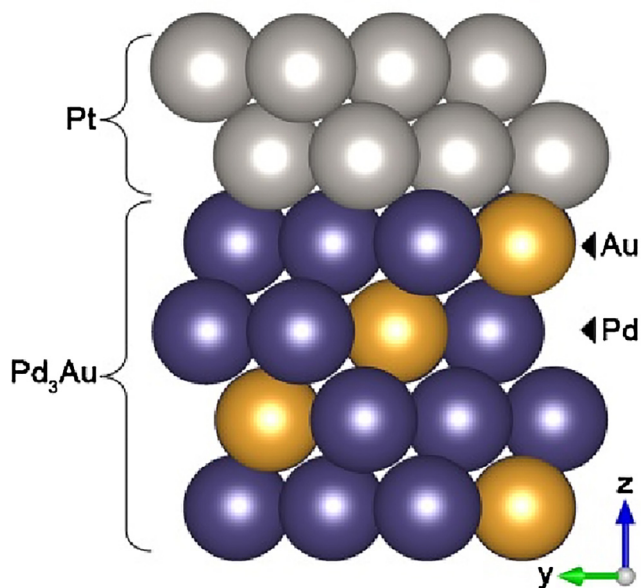

Fig. 6. Side view of Pt/Pd$_3$Au(111). Each layer of Pd$_3$Au(111) consists of three Pd atoms and one Au atom.

3.3. DFT calculations

The segregation of Au atoms from the bulk Pd$_3$Au(111) core to the upper layers was modeled using modified Pt/Pd$_3$Au(111) surfaces, as shown in Fig. 5. Depending on the location of the Au atoms, the modified Pt/Pd$_3$Au(111) surfaces were classified as Level I (a, b, c, d) or II (e, f, g, h), where the Au atoms migrate to the top layer of Pd$_3$Au(111) and the Pt sublayer, respectively. The Pt vacancy formation energies (E_{vac}) of the Pt(111) and Pt/Pd$_3$Au(111) surfaces were 1.01 and 0.96 eV (or 0.85 eV, depending on the vacancy loca-

tion), respectively. However, as the sublayer Au atoms segregated towards the surface in Fig. 5, E_{vac} tended to increase. In particular, the E_{vac} value became even greater than that of Pt(111), when all the four Au atoms migrated up to the 2nd top Pt layer (Fig. 5e) with E_{vac} of 1.20 eV), implying that the stability of Pt/Pd$_3$Au(111) can be expected to be better than that of Pt(111), when the Au atoms are fully segregated from the bulk to the Pt layers.

The enhanced surface stability of the modified Pt/Pd$_3$Au(111) system (Fig. 5e) may be attributed to the accumulated charge polarization in the top Pt layer. The segregation of Au atoms causes electron transfer from the sublayer Au atoms to the top Pt layers. To prove this, Bader charge calculations were performed for the systems in Fig. 5e, h)(Table S5), **6**(Pt/Pd$_3$Au) with a single Pt vacancy site, as described in Fig. S14. As indicated in Table S5, E_{vac} increased as the Bader charge of the surface Pt atoms increased whereas it decreased with increase in the Bader charge of Au. This result supports the idea that the segregation of Au atoms may contribute to increase in the stability of the Pt/Pd$_3$Au(111) surface, by transferring electronic charges to the top Pt surface.

The various shell layers of the core-shell nanocatalysts were shown to have different characteristics. The durability and stability of the nanocatalysts after ADT were demonstrated not only in the physical analysis by Cs-STEM, but also in the electrochemical catalytic activity measurements. Although the monolayer Pt shell exhibited the greatest Pt-based mass activity, it lacked durability. owing to Pd dissolution. Furthermore, the core@Pt[3]/C nanocatalyst was shown to experience unfavorable Pt usage, owing to excessive Pt dissolution. Therefore, an optimal shell layer is achieved in the core@Pt[2]/C nanocatalyst, with adequate activity and durability. Interestingly, in the core@Pt[2] and [3]/C samples, Au was found to be segregated from the core. Through Cs-STEM and CO$_{2ad}$ oxidation measurements, the core-shell structure was shown to be rearranged during ADT. In addition, the DFT calculations showed that the stability and durability were enhanced, demonstrating that the electron transfer resulting from Au segregation from the sublayer to the top Pt layer was beneficial from

the point of view of stability and durability. This study suggests that core-shell structure nanocatalysts could be synthesized by the chemical reduction method and the number of shell layers can be optimized, in order to achieve a stable and durable nanocatalyst.

4. Conclusion

Nanocatalysts with core-shell structure composed of a Pd_3Au core and Pt shell were successfully synthesized by the chemical reduction method and the Pt shell layer was optimized to enhance the durability and structural stability of the catalyst. The catalytic activities were determined for Pt shells with different numbers of layers. In addition, catalytic activities were also examined before and after ADT. The core@Pt[1]/C nanocatalyst was found to exhibit good mass activity. However, the dissolution of Pd during ADT was expected to affect the core-shell structure. Although the core@Pt[3]/C nanocatalyst with three Pt shell layers exhibited better ORR performance compared to the other samples, the core@Pt[2]/C nanocatalyst was considered to be more optimal, owing to Pt dissolution during the ADT in the cased of the former. The Pt-based mass activity was ranked in the following order: core@Pt[1]/C > core@Pt[2]/C > core@Pt[3]/C > commercial Pt/C. However, the difference in the mass activity of core@Pt[2]/C before and after ADT (−3.01%) was lower than the corresponding values for core@Pt[1]/C (−9.75%), core@Pt[3]/C (−18.08%), and commercial Pt/C (−38.73%), highlighting the stability of core@Pt[2]. In addition, the difference in the Pt-based specific activity before and after ADT for core@Pt[2]/C (6.61%) was comparable or lower than core@Pt[3]/C (6.21%), core@Pt[1]/C (−22.06%), and commercial Pt/C (−26.72%). We suggest that the core-shell structure of the nanocatalyst with optimized Pt shell layer synthesized *via* chemical reduction is active and durable during ADT. The results obtained in this study highlight the importance of this highly promising method for improving one of the key problems in fuel cell research and will be useful in accelerating the commercialization of fuel cells.

Acknowledgments

Appendix A. Supplementary data

Supplementary data associated with this article can be found, in the online version, at http://dx.doi.org/10.1016/j.apcatb.2017. 01.073.

References

[1] N.M. Markovic, T.J. Schmidt, V. Stamenkovic, P.N. Ross, Fuel Cells 1 (2001) 105.
[2] R.R. Adzic, J. Zhang, K. Sasaki, M.B. Vukmirovic, M. Shao, J.X. Wang, A.U. Nilekar, M. Mavrikakis, F. Uribe, Top. Catal. 46 (2007) 249.
[3] T. Goshi, M.B. Vukmirovic, F.J. DiSalvo, R.R. Adzic, J. Am. Chem. Soc. 132 (2010) 906.
[4] K. Sasaki, H. Naohara, Cai, Y, Y.M. Choi, P. Liu, M.B. Vukmirovic, J.X. Wang, R.R. Adzic, Angrew. Chem. Int. Ed. 49 (2010) 8607.
[5] L. Yang, M.B. Vukmirivic, D. Su, K. Sasaki, J.A. Herron, M. Mavrikakis, S. Liao, R.R. Adzic, J. Phys. Chem. C 117 (2013) 1748.
[6] P. Strasser, S. Koh, J. Greeley, Phys. Chem. Chem. Phys. 10 (2008) 3670.
[7] J. Greeley, I.E.L. Stephens, A.S. Bondarenko, T.P. Johansson, H.A. Hansen, T.F. Jaramillo, J. Rossmeisl, I. Chorkendorff, J.K. Norslov, Nat. Chem. 1 (2009) 552.
[8] U.A. Pailis, A. Wokaun, G.G. Scherer, T.J. Schmidt, V. Stamenkovic, V. Radmilovic, N.M. Markovic, P.N. Ross, J. Phys. Chem. B 106 (2002) 4181.
[9] H.T. Duong, M.A. Rigsby, W.P. Zhou, A. Wieckowski, J. Phys. Chem. C 111 (2007) 13460.
[10] C. Wang, D. van der Vilet, K.C. Chang, H.D. You, D. Strmcnik, J.A. Schlueter, N.M. Markovic, V.R.J. Stamenkivic, Phys. Chem. C 113 (2009) 19365.
[11] Z. Pu, Q. Liu, C. Tang, A.M. Asiri, A.H. Qusti, A.O. Al-Youbi, X. Sun, J. Power Source 257 (2014) 170.
[12] R. Ning, C. Ge, Q. Liu, A.M. Asiri, K.A. Alamry, C.M. Li, X. Sun, Carbon 78 (2014) 60.
[13] R. Ning, J. Tian, A.M. Asiri, A.H. Qusti, A.O. Al-Youbi, X. Sun, Langmuir 29 (2013) 13146.
[14] V.R. Stamenkovic, B. Fowler, B.S. Mun, G.F. Wang, P.N. Ross, C.A. Lucas, N.M. Markovic, Science 315 (2007) 493.
[15] J.L. Zhang, M.B. Vukmirovic, Y. Xu, M. Mavrikakis, R.R. Adzic, Angew. Chem. Int. Ed. 44 (2005) 2132.
[16] J.X. Wang, H. Inada, L.J. Wu, Y.M. Zhu, Y.M. Choi, O. Liu, W.P. Zhou, R.R. Adzic, J. Am. Chem. Soc 131 (2009) 17298.
[17] C. Xu, Y. Liu, Q. Hao, H.J. Duan, Mater. Chem. A 1 (2013) 13542.
[18] J. Qiao, R. Lin, B. Li, J. Ma, J. Liu, Electrochimi. Acta 55 (2010) 8490.
[19] W. Du, N.A. Deskins, D. Su, X. Teng, ACS Catal. 2 (2012) 1226.
[20] K. Lee, L. Zhang, J. Zhang, J. Power Sources 170 (2007) 291.
[21] G. Liu, H. Zhang, J. Phys. Chem. C 112 (2008) 2058.
[22] A. Sarkar, A.V. Murugan, A.J. Manthiram, Mater. Chem. 19 (2009) 159.
[23] N.N. Kariuki, X. Wang, J.R. Mawdsley, M.S. Ferrandon, S.G. Niyogi, J.T. Vaughey, D. Myers, J. Chem. Mater. 22 (2010) 4144.
[24] Y. Xing, Y. Cai, M.B. Vukmirovic, W.P. Zhou, H. Karan, J.X. Wang, R.R. Adzic, J. Phys. Chem. Lett. 1 (2010) 3238.
[25] T. Bligaard, J.K. Norskov, Electrochim. Acta 52 (2007) 5512.
[26] L. Garbow, Y. Xu, M. Mavrikakis, Phys. Chem. Chem. Phys. 8 (2006) 3369.
[27] J.R. Kitchin, J.K. Norskov, M.A. Bateau, J.G. Chen, J. Chem. Phys. 120 (2004) 10240.
[28] A.U. Nielkar, M. Mavrikakis, Surf. Sci. 602 (2008) L89.
[29] K. Sasaki, H. Naohara, Y.M. Choi, W.F. Chen, P. Liu, R.R. Adzic, Nat. Commun. 3 (2012) 1115.
[30] L. Zhang, R. Iyyamperumal, D.F. Yancey, R.M. Crooks, G. Henkelman, ACS Nano 7 (2013) 9168.
[31] F. Hasche, M. Zezaslan, r.P. Strasse, J. Electrochem. Soc. 159 (2012) B24.
[32] N. Oezaslan, F. Hasche, P. Strasser, J. Power Sources 196 (2011) 5240.
[33] S. Koh, P. Strasser, J. Am. Chem. Soc. 129 (2007) 12624.
[34] M. Oezaslan, F. Hasche, P. Strasser, J. Electrochem. Soc. 159 (2012) B394.
[35] M. Oezaslan, F. Hasche, P. Strasser, J. Electrochem. Soc. 159 (2012) B444.
[36] F. Hasche, M. Oezaslan, r.P. Strasse, ECS Trans. 41 (2011) 1079.
[37] C. Wang, M. Chi, G. Wang, D. van der Vliet, D. Li, K. More, H. Wang, J.A. Schlueter, N.M. Markovic, V.R. Stamenkovic, Adv. Funct. Mater. 21 (2011) 147.
[38] L. Gan, M. Heggen, S. Rudi, P. Strasser, Nano Lett. 12 (2012) 5423.
[39] K.J.J. Mayrhofer, V. Juhart, K. Hartl, M. Hanzlik, M. Arenz, Angew. Chem. Int. Ed. 48 (2009) 3529.
[40] C. Wang, G. Wang, D. van der Vliet, K. Chang, N.M. Markovic, V.R. Stamenkovic, Phys. Chem. Chem. Phys. 12 (2010) 6933.
[41] M.H. Lee, J.S. Do, J. Power Sources 188 (2009) 353.
[42] C. Wang, D. van der Vliet, K.L. More, N.J. Zaluzec, S. Peng, S. Sun, H. Daimon, G. Wang, J. Freely, J. Pearson, A.P. Paulikas, G. Karaoetrov, D. Strmcnik, N.M. Markovic, V.R. Stamenkovic, Nano Lett. 11 (2011) 919.
[43] M. Shao, K. Sasaki, N.S. Marinkovic, L. Zhang, R.R. Adzic, Electrochem. Commun. 9 (2007) 2848.
[44] W.P. Zhou, X. Yang, M.B. Vukmirovic, B.E. Koel, J. Jiao, G. Peng, M. Mavrikakis, R.R. Adzic, J. Am. Chem. Soc. 131 (2009) 12755.
[45] J. Zhang, Y. Mo, M.B. Vukmirovic, R. Klie, K. Sasaki, R.R. Adzic, J. Phys. Chem. B 108 (2004) 10955.
[46] S.J. Hwang, S.J. Yoo, J. Shin, Y.H. Cho, J.H. Jang, E. Cho, Y.E. Sung, S.W. Nam, S.C. Lee, S.K. Kim, Sci. Rep. 3 (2013) 1309.
[47] G. Kresse, J. Hafner, Ab initio molecular dynamics for liquid metals, Phys. Rev. B 47 (1993) 558–561.
[48] G. Kresse, J. Hafner, Ab initio molecular-dynamics simulation of the liquid-metal amorphous-semiconductor transition in germanium, Phys. Rev. B 49 (1994) 14251.
[49] G. Kresse, J. Furthmüller, Efficient iterative schemes for ab initio total-energy calculations using a plane-wave basis set, Phys. Rev. B 54 (1996) 11169–11186.
[50] G. Kresse, J. Furthmüller, Efficiency of ab-initio total energy calculations for metals and semiconductors using a plane-wave basis set, Comput. Mater. Sci. 6 (1996) 15–50.
[51] P.E. Blöchl, Projector augmented-wave method, Phys. Rev. B 50 (1994) 17951–17953.
[52] G. Kresse, D. Joubert, From ultrasoft pseudopotentials to the projector augmented-wave method, Phys. Rev. B 59 (1999) 1758–1775.
[53] J.P. Perdew, K. Burke, M. Ernzerhof, Generalized gradient approximation made simple, Phys. Rev. Lett. 77 (1996) 3865–3868.
[54] H.J. Monkhorst, J.D. Pack, Special points for Brillouin-zone integrations, Phys. Rev. B 13 (1976) 5188–5192.
[55] M. Methfessel, A.T. Paxton, High-precision sampling for Brillouin-zone integration in metals, Phys. Rev. B 40 (1989) 3616–3621.
[56] H.R. Choi, H. Woo, S. Jang, J.Y. Cheon, C. Kim, J. Park, K.H. Park, S.H. Joo, ChemCatChem 4 (2012) 1587.
[57] T.Y. Jeon, S.J. Yoo, H.Y. Park, S.K. Kim, S. Lim, D. Peck, D.H. Jung, Y.E. Sung, Langmuir 28 (2012) 3664.
[58] D. Zhao, B.Q. Xu, Angew. Chem. Int. Ed. 45 (2006) 4955.

[59] K.S. Lee, S.J. Yoo, D. Ahn, T.Y. Jeon, K.H. Choi, I.S. Park, Y.E. Sung, Langmuir 27 (2011) 3128.
[60] P.A. Nascente, S.G.C. P.; de Castro, R. Landers, G.G. Kleiman, Phys. Rev. B 43 (1991) 4659.
[61] S.Y. Lee, N. Jung, J. Cho, H.Y. Park, J. Ryu, I. Jang, H.J. Kim, E. Cho, Y.H. Park, H.C. Ham, J.H. Jang, S.J. Yoo, ACS Catal. 4 (2014).
[62] M. Oezaslan, F. Hasche, P. Strasser, J. Phys. Chem. Lett. 4 (2013) 3273.
[63] H. Li, G. Sun, Q. Jiang, M. Zhu, S. Sun, Q. Xin, J. Power Sources 172 (2007) 641.
[64] M. Grden, A. Paruszewska, A. Czerwinski, J. Electroanal. Chem. 502 (2001) 91.
[65] T.Y. Jeon, S.J. Yoo, Y.H. Cho, H.Y. Park, Y.E. Sung, Electrochem. Commun. 28 (2013) 114.